Importance of geometric effects in scaling up energy-efficient plasma-based nitrogen fixation†

Ivan Tsonev[*‡a], Hamid Ahmadi Eshtehardi[‡a,b], Marie-Paule Delplancke[b], Annemie Bogaerts[a]

Abstract

Despite the recent promising potential of plasma-based nitrogen fixation, the technology faces significant challenges in efficient upscaling. To tackle this challenge, we investigate two reactors, i.e., a small one, operating in a flow rate range of 5 – 20 ln/min and current range of 200 – 500 mA, and a larger one, operating at higher flow rate (100 – 300 ln/min) and current (400 – 1000 mA). Both reactors operate in a pin-to-pin configuration and are powered by direct current (DC) from the same power supply unit, to allow easy comparison and evaluate the effect of upscaling. In the small reactor, we achieve the lowest energy cost (EC) of 2.8 MJ/mol, for a NO_x concentration of 1.72%, at a flow rate of 20 ln/min, yielding a production rate (PR) of 33 g/h. These values are obtained in air; in oxygen-enriched air, the results are typically better, at the cost of producing oxygen-enriched air. In the large reactor, the higher flow rates reduce the NO_x concentration due to lower SEI, while maintaining a similar EC. This stresses the important effect of the geometrical configuration of the arc, which is typically concentrated in the center of the reactor, resulting in limited coverage of the reacting gas flow, and this is identified as the limiting factor for upscaling. However, our experiments reveal that by changing the reactor configuration, and thus the plasma geometry and power deposition mechanisms, the amount of gas treated by the plasma can be enhanced, leading to successful upscaling. To obtain more insights in our experiments, we performed thermodynamic equilibrium calculations. First of all, they show that our measured lowest EC closely aligns with the calculated minimum thermodynamic equilibrium at atmospheric pressure. In addition, they reveal that the limited NO_x production in the large reactor results from the contracted nature of the plasma. To solve this limitation, we let the large reactor operate in so-called torch configuration. Indeed, the latter enhances the NO_x concentrations compared to the pin-to-pin configuration, yielding a PR of 80 g/h at an EC of 2.9 MJ/mol and NO_x concentration of 0.31%. This illustrates the importance of reactor design in upscaling.

1. Introduction

The Haber-Bosch (HB) process, currently used for industrial fertilizer production, is responsible for the emission of more than 300 Mt of CO_2 annually [1]. The transition to a carbon-free economy creates the urgent need to find an alternative for the production of chemical fertilizers. Electrification of the chemical industry is one of the key challenges of the 21st century. Plasma-based nitrogen fixation (NF) toward NO_x has

[a.] Research group PLASMANT, University of Antwerp, Department of Chemistry, Universiteitsplein 1, BE-2610 Wilrijk-Antwerp, Belgium.
[b.] Research group 4MAT, Ëcole polytechnique de Bruxelles, 50 Roosevelt Av., CP 165/63, 1050 Brussels, Belgium.
* Email: Ivan.Tsonev@uantwerpen.be
‡ Shared first author
† Electronic supplementary information (ESI) available.

attracted significant interest in the past few years, due to its compatibility with renewable electricity and its turn-key capabilities to convert renewable energy into chemicals and fuels [2,3]. NO and NO_2 (i.e., NO_x) can be produced via plasma-based NF from air. The produced NO_x can then be dissolved in water to form HNO_3. Finally, this acidic solution can react with NH_3, forming ammonium nitrate (NH_4NO_3), which is a fertilizer with high nitrogen content (35%) per mass [4]. Over the past century, the HB process has been significantly optimized, leading to a very low energy cost (EC) for NF into NH_3 (0.5 MJ/mol) [5]. This also presents the biggest challenge for the plasma-based process: the EC depends on both the specific energy input (SEI) and NO_x concentration: a higher SEI typically yields a higher NO_x concentration, but when the NO_x concentration does not rise more than the SEI, the corresponding EC will rise as well. In other words, upon rising SEI, the NO_x concentration should rise faster to keep a good EC.

Several plasma discharges have been explored already for NO_x production. The energy cost of NO_x production in various plasma systems was compared in a techno-economic study by Rouwenhorst et al., who concluded that if the energy cost is reduced to 1.0-1.5 MJ/mol, plasma technology can compete with the current industrial combination of the Haber-Bosch process with the Ostwald process [5,6]. Additionally, Liu et al. reviewed the reaction pathways, energy flow and performance of different plasma reactors for NO_x production from N_2/O_2 mixtures [7]. They discussed four different mechanisms playing a key role toward NO_x production, i.e., with dominant role of either electronically or vibrationally excited N_2 molecules, or a combination of both, and a dominant role of $N(^2D)$ excited atoms, dependent on the type of discharge generated in the plasma reactor. Furthermore, they also explained the energy flow distributions, i.e., how much energy is going into heat vs chemical reactions, and the main heating mechanisms. Finally, they concluded that there is a need to develop new plasma devices where one can independently adjust the electron and gas temperature, to gain more insight in the mechanisms [7]. The reported NO_x concentration and EC for plasma-based NO_x production at various SEI values for different plasma types are summarized in Figure 1. Birkeland and Eyde were the first to develop an industrial thermal plasma reactor for NF [8,9], and achieved an NO production of 1-2% with an EC of 2.4-3.1 MJ/mol. Krop and Pollo reported an NO production of 4.7% at an EC of 3.5 MJ/mol, in an electric arc plasma reactor with water injection [10]. Bian et al. studied NO_x production from air in a water jet discharge and reported a NO_x concentration of 1% with an EC of 47 MJ/mol [11]. For radio frequency (RF) plasmas, NO_x concentrations around 2-900 ppm (hence, below 0.01%), with EC ranging from 363 to 2133 MJ/mol, were reported [12,13]. Likewise, NO_x concentrations between 0.01 and 0.6% have been reported in dielectric barrier discharge (DBD) plasmas, with EC between 21-540 MJ/mol [14–17]. Inductively coupled plasmas (ICP) have been reported to produce NO_x concentrations between 5.5 and 19%, but with EC ranging from 1921 to 26451 MJ/mol [18]. Microwave (MW) plasmas at reduced pressure (50 torr) showed an NO production between 6-20% with an EC of 0.2-0.9 MJ/mol; however, these record values were not reproduced since then [19–21]. Direct current (DC) spark

discharges yielded NO_x concentrations ranging from 7 to 6000 ppm (i.e., up to 0.6%) with EC between 0.4 and 20 MJ/mol [22–24]. Vervloessem et al. showed that in a pulsed spark discharge, the EC of NO_x production from air can drop to a mere 0.4 MJ/mol, close to the theoretical minimum, but indeed, at the expense of a very low NO_x concentration (300 ppm) [22]. In recent years, there are various papers in literature on gliding arc (GA) plasmas, producing NO_x concentrations in the range of 0.001 to 6.5%, with EC between 1.8 and 15 MJ/mol [14,25–33]. For instance, Jardali et. al. performed studies with a rotating gliding arc (RGA) plasma, achieving an EC of 2.5 MJ/mol with an appreciable NO_x concentration of 5.2% in oxygen-enriched air [25]. This result was further improved by the application of an effusion nozzle by Van Alphen et al., yielding 2.1 MJ/mol EC and an NO_x concentration of 5.9% in oxygen-enriched air [26]. Very recently, we have shown that increasing the pressure leads to a further improvement of the performance in an RGA reactor, with EC as low as 1.8 MJ/mol, NO_x concentration of 4.8%, and PR of 69 g/h, in oxygen-enriched air, at a pressure of 3 barg [27]. MW plasmas at atmospheric pressure also produce NO_x concentrations in the range of 0.32 to 3.81% with EC between 2 to 4.5 MJ/mol [34,35]. For example, impressive results were achieved by Kelly and Bogaerts, where a MW plasma at atmospheric pressure with oxygen-enriched air gave an EC of 2.0 MJ/mol with NO_x concentration of 3.8% and high production rate (PR) of ca. 86 g/h [34]. Notably, the performance was better at higher power and flow rate, showing the promise for upscaling. Pei et al. performed studies on NF with a DC glow discharge plasma in air and reported a NO_x concentration of 0.7% with an EC of 2.8 MJ/mol [36]. It is clear from the above that thermal reactions, which dominate in (near-)thermodynamic equilibrium plasmas, give rise to efficient dissociation of N_2 and O_2 molecules. On the other hand, electron impact reactions are important in non-equilibrium plasmas. Direct electron impact dissociation (which often proceeds through electronic excitation) and ionization typically require more energy than strictly needed for bond breaking, and this explains by non-equilibrium plasmas, such as DBD, exhibit a high energy cost. However, at lower electron energy, electron impact reactions lead to vibrational excitation of N_2 and O_2 molecules, and the stored energy in the vibrationally excited levels can be used to overcome the energy barrier of dissociation, and of NO formation. In warm plasmas, both vibrational-induced dissociation and thermal reactions can occur simultaneously, depending on the conditions[37].

Taken together, this literature overview shows that among the different plasma types, warm plasmas, such as GA, MW and DC glow discharge plasmas, have the best performances for plasma-based NO_x production at atmospheric pressure. This is indeed attributed to the highly efficient thermal reactions occurring due to the high temperatures (> 3000 K) achieved in these plasmas [5,38].

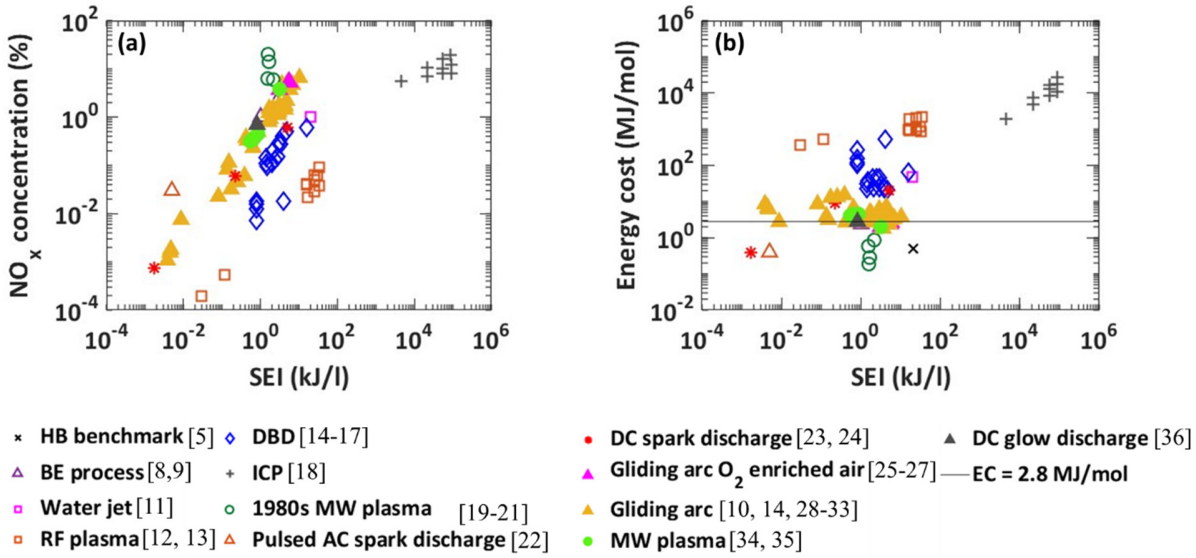

Figure 1. Reported NO_x concentration (a) and EC (b) of plasma-based NO_x production, as a function of SEI in various plasma reactors. Original references: 1980s low pressure MW plasma, MW plasma at atmospheric pressure, GA, RF plasma, DBD, ICP, spark discharge, and DC glow discharge. The horizontal line in (b) corresponds to the EC of 2.74 MJ/mol, which is the minimum thermodynamic equilibrium EC for atmospheric pressure NF (as discussed further in this paper). Only some low-pressure plasmas produce a lower EC, demonstrating they are characterized by thermodynamic non-equilibrium. Among the atmospheric pressure plasmas (more suitable for upscaling and industrial implementation), warm plasmas, such as GA, MW and DC glow discharge plasmas (all indicated with solid symbols), show the best performance in terms of both NO_x concentration and EC (close to the thermodynamic equilibrium limit), as explained in the text.

Except for the Birkeland-Eyde process, all other reported plasma processes have been operated in lab scale reactors. Indeed, scaling up of plasma-based NF with a low EC and high NO_x concentration remains a big challenge for the industrialization of this process.

In the present work, we try to tackle this challenge by developing a low current, high flow rate plasma reactor and comparing the results to a smaller counterpart. In this way, we are able to scan a large SEI range and investigate for the first time, in a systematic way, the potential of scaling up the NF process. The high gas flow rates, up to 300 ln/min, allow to increase the PR, even at low NO_x concentrations. This effect, in combination with elevated pressure, can potentially enhance the industrial applicability of plasma-based NF.

Last but not least, in order to explain our experimental results, we apply thermodynamic equilibrium calculations, to estimate the flow rate passing through the region with elevated temperature, as well as the gas temperature. This gives us deeper insights in the limitations that need to be overcome for successful upscaling. To the best of our knowledge, this is the first report on scaled-up plasma-based NF since the Birkeland-Eyde process.

2. Experimental setup

In order to test the effects of upscaling, we used two different plasma reactors in this work, i.e., a large one and its smaller counterpart, but based on the same operating principle, i.e., pin-to-pin configuration, powered by the same DC current-controlled power supply and operating in the low-current arc regime. Arc discharges are characterized by electron emission at the cathode being either field or thermionic emission or a combination of both [39]. Although at very low currents (< 50 mA) they can exhibit non-equilibrium effects, in the current range of 200 – 1000 mA (as in our study), arc discharges in air are typically in local thermodynamic equilibrium [40]. This current range, in combination with a wide range of flow rates, being applicable to either the small or large reactor, allows us to cover a wide SEI range of 0.1 – 7.6 kJ/l. The small reactor operates from 0.9 – 7.6 kJ/l, i.e., a high SEI region. The large reactor only operates at lower SEI, i.e., 0.1 – 1 kJ/l, because of the high flow rates, but not very high power (limited by the power supply unit (PSU); see below). Besides the pin-to-pin configuration (like its smaller counterpart), it can also operate in another, so-called torch configuration (see below).

2.1. Small reactor

A schematic representation of the small reactor is presented in Figure 2.

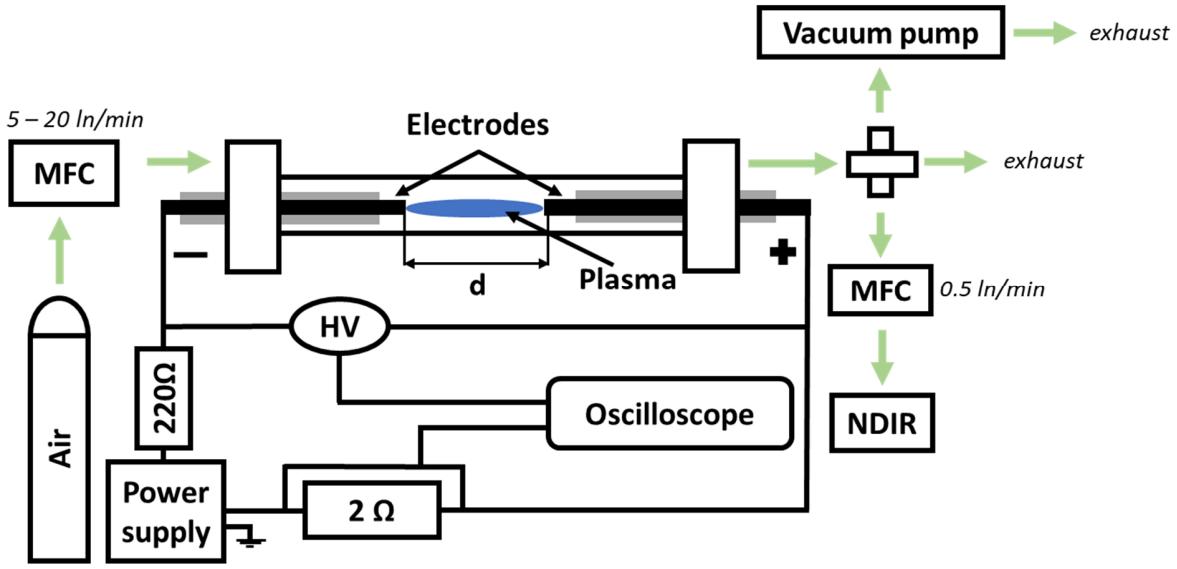

Figure 2. Schematic representation of the small reactor, with plasma (indicated in blue) ignited between the two opposing electrodes (indicated in black). The actual picture of the small reactor is illustrated in SI (Figure S1 a).

A compressed air cylinder was connected to a mass flow controller (MFC, Bronkhorst F-210CV), which supplied the gas flow to the reactor (5, 10, 15, 20 ln/min at STP conditions). The mass flow rate is indicated

in ln/min (normal liters per minute), which refers to reference conditions of 0 ºC and 1 bar, consistent with the definition of the MFC manufacturer, who defines normal liters at 0 °C.

The plasma was generated between two cylindrical stainless-steel electrodes (8 mm in diameter, indicated in black in Figure 2) placed inside a quartz tube with 16 mm inner and 20 mm outer diameter. The electrodes were insulated from the body of the reactor by an Al_2O_3 tube placed around them (indicated in grey in Figure 2). The distance between both electrodes (d in Figure 2) was varied between 7 and 14 cm. The reactor volume is 14.1 and 28.2 cm^3 for d = 7 and 14 cm, respectively. Including a swirl flow in the small reactor is possible, and it will insulate the plasma from the walls and also change the plasma dynamics for higher flow rates (i.e., larger than 10 ln/min). This will be beneficial when going to higher power, and hence higher SEI, but our laboratory currently has no appropriate power supplies which can supply higher than 1 A of current.

The concentration of NO and NO_2 was measured using a non-dispersive infrared (NDIR) detector (Emerson, Rosemount X-stream enhanced XEGP continuous gas analyzer). The NDIR was calibrated using calibration gases (16.02 vol% NO in He, 7.80 vol% NO_2 in He) purchased from Praxair, and the calibration procedure is explained in the SI, section S2. Although the calibration gases are in He, this calibration is still valid for NO_x production in air, because they are mimicking the target gases absorption characteristics due to the inert nature of helium, and the fact that it does not interfere with the absorption features of NO and NO_2. Note that the measurement device could only detect NO and NO_2 (which we denote here collectively as NO_x). Each experiment was conducted three times to obtain the standard deviation. The current applied to the reactor was varied between 200 and 500 mA. Details of the PSU are mentioned below.

2.2. Large reactor

As mentioned above, the large reactor can operate both in a pin-to-pin and torch configuration, with the plasma being stabilised by a swirling flow. Experiments without swirling flow were also conducted, but the plasma stability was significantly reduced. A schematic of the experimental setup of the large reactor in pin-to-pin configuration is presented in Figure 3.

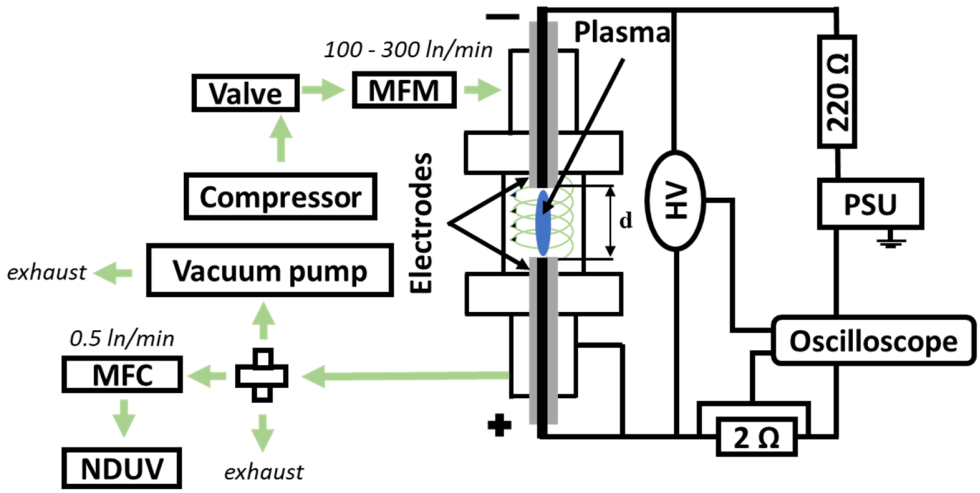

Figure 3. Schematic representation of the large reactor, with plasma (indicated in blue) ignited between the two opposing electrodes (indicated in black) and the swirling flow around the plasma (indicated in green). The actual picture of the large reactor is illustrated in SI (Figure S1 b).

The reactor consists of two WLa electrodes with diameter of 30 mm, encased in 40 mm Si_3N_4 insulation (indicated in black and grey in Figure 3, respectively). The electrodes are placed within a stainless-steel tube with inner diameter of 63 mm and outer diameter of 73 mm. The distance between both electrodes (d in Figure 3) was also varied between 7 and 14 cm. The reactor volume is 218.2 and 436.4 cm^3 for d = 7 and 14 cm, respectively, hence more than 10 times larger than its smaller counterpart. When investigating the reactor in torch configuration (see schematic diagram in Supporting Information (SI), Figure S3), the bottom electrode was removed, and the reactor body acted as grounded electrode. Note that we evaluate this torch configuration to overcome the limitations of the pin-to-pin configuration, as explained in the Results and Discussion section.

An air compressor is connected to a control valve, which in turn is connected to the reactor through a mass flow meter (MFM) (IFM SD6500), which supplies the flow rate to a helical swirl generator. The current was varied between 300 and 1000 mA, and the flow rate of air between 100 ln/min and 300 ln/min. The PSU (at lab scale) did not allow to apply power above 2500 W, or current above 1000 mA. This, in combination with the high flow rates, is the reason why this reactor only operates in the low SEI region of 0.1 – 1 kJ/l, as mentioned above. The NO and NO_2 concentrations were measured by non-dispersive ultraviolet spectroscopy (NDUV) using a WiTec ULTRA-Sens NOx AK100 TBH gas analyzer, calibrated similarly to NDIR as described above. Note that the gas analyzer could again only detect NO and NO_2 (collectively denoted as NO_x). The reason for using a different gas analyzer for the large reactor is that the NDIR detector, used for the small reactor, is not accurate for measuring NO_x concentrations less than 1%

(i.e., in the ppm range), while the produced NO_x concentrations in the large reactor are always below 0.5% (see below).

Note that the breakdown voltage of air, permitting the discharge ignition at atmospheric pressure, is 3 kV/mm. For all experimental conditions (i.e., small reactor and large reactor in pin-to-pin and torch configuration), we first vacuum the system, and apply an initial potential difference of 10 kV between the electrodes. This results in gas breakdown and formation of an arc discharge. Upon ignition, the voltage drops, e.g., to values between 0.5-2.5 kV for the electrode distance of 14 cm. The pressure is then increased to atmospheric, and finally, the vacuum pump is removed from the system.

2.3. Definition of the performance metrics

For both reactors, the voltage was measured with a high voltage probe (HV) (Tektronix P6015A) and the current was obtained by measuring the voltage drop across a shunt resistor with 2 Ω resistance. Both signals were recorded with a two-channel oscilloscope (Keysight InfiniiVision DSOX1102A). The current was supplied with a current-controlled PSU (Technix SR12KV-10KW) with negative output polarity, for both reactors.

The plasma power was calculated by averaging the instantaneous power measurements as:

$$P\ [W] = \frac{1}{n}\sum_{i=1}^{n} V_i \times I_i = \frac{1}{n}\sum_{i=1}^{n} V_{plasma_i} \times \frac{V_{shunt_i}}{R_{shunt}} \quad (1)$$

Where n is the number of recorded points (in the order of thousands, depending on the oscilloscope settings), V_{plasma_i} is the voltage drop across the plasma discharge, V_{shunt_i} is the voltage drop across the shunt resistor and R_{shunt} is the resistance of the shunt resistor. In order to calculate the power, three scopes are taken and then averaged for each of the experimental conditions. Examples of the voltage and current scopes are presented in SI (Figure S4). For the small reactor, we observed a periodic signal, oscillating around the current value set on the power supply and the burning voltage. For the large reactor, we observed a rather random behaviour, with longer periods of stability but stronger voltage and current peaks, indicating restriking (see SI for details).

The SEI is calculated from the plasma power and the total gas flow rate as:

$$SEI\ \left[\frac{kJ}{l}\right] = \frac{P\ [W]\ \times\ 60\ \left(\frac{s}{min}\right)}{flow\ rate\ [ln/min]} \times 10^{-3}\ \left[\frac{kJ}{J}\right] \quad (2)$$

The EC is calculated from the total measured NO_x ($NO + NO_2$) concentration, the power and flow rate (which both define the SEI), as:

$$EC\left[\frac{MJ}{mol}\right] = \frac{P\,[W] \times 22.4\left(\frac{ln}{mol}\right) \times 60\left(\frac{s}{min}\right) \times 100[\%]}{total\ NO_x\ concentration\ [\%] \times flow\ rate\ [ln/min]} \times 10^{-6}\left[\frac{MJ}{J}\right] \quad (3)$$

Where 22.4 ln/mol is the molar volume at normal conditions as explained above.

The PR is calculated as follows:

$$PR_{NO_x}\left[\frac{g}{h}\right] = \frac{\left(x_{NO} \times 30\left[\frac{g}{mol}\right] + x_{NO_2} \times 46\left[\frac{g}{mol}\right]\right) \times flow\ rate\ [ln/min]}{22.4\left[\frac{ln}{mol}\right]} \times 60\left[\frac{min}{h}\right] \quad (4)$$

Where x_{NO} and x_{NO_2} are the fraction of NO and NO_2 in the gas flow after the plasma. In eqs. 3 and 4, the change of the volume due to the stoichiometry of NO_2 formation is neglected, because the main product is NO, while NO_2 is formed at very low amounts (less than 2 % for all conditions). The NO_x concentration was measured after the reactor performance has achieved steady state, and there are no changes in concentration as a function of time. In addition, each of the experiments was also conducted three times, in order to reduce the uncertainty. The error bars are present in all figures, but in some cases they are too small to be visible.

3. Model description

To gain better insights in our experimental results, and based on the fact that, according to literature, plasmas operating at currents higher than 200 mA are in local thermodynamic equilibrium (LTE) [40], we developed a model based on thermodynamic equilibrium considerations. The EC associated with thermodynamic equilibrium was calculated by estimating the energy needed to heat the gas in the temperature range of 300 – 6000 K, which is a sufficiently wide range for plasmas at atmospheric pressure. We used the following relation:

$$q = \int_{300}^{T_2} C_p(T)dT \quad (5)$$

Where q is the energy needed to heat one kg of gas, $Cp(T)$ is the heat capacity as a function of temperature (here in J kg^{-1} K^{-1}), and T_2 is the temperature to which we are heating the gas. We can then multiply this energy by the thermodynamic equilibrium NO fraction in the gas for a given temperature T_2 to determine the EC for NO formation as a function of temperature. Considering that, according to this approach, the EC is a function of NO mass flow rate and not the total gas flow rate fed to the reactor, we can easily correlate the experimental EC with the calculated equilibrium values, as a function of temperature, and obtain a rough estimation of the plasma temperature. Following the same idea, we can calculate the power needed to heat a given mass flow of gas to a given temperature T_2:

$$P = \dot{m} \int_{300}^{T_2} C_p(T) dT \tag{6}$$

Where P is the power needed to heat the gas, and $\dot{m}$ is the mass flow rate (in kg/s, but later converted to ln/min to be consistent with the experimental flow rates). We note that if the power is divided by the flow rate, we obtain the SEI. The results of the model can then be expressed as a function of SEI, but for clarity we use power and flow rate, as these are macroscopic parameters typically used as input in the experiments. The heat capacity of the gas as a function of temperature was obtained from a zero-dimensional model for calculating the equilibrium composition as a function of temperature using COMSOL Multiphysics 6.0 [41]. The model includes five species: N_2, O_2, N, O, NO. NO_2 is not included in the model because oxidation from NO to NO_2 happens in the post-plasma region [33], and our experiments reveal anyway that NO_2 is formed at less than 2% of the NO concentration for all conditions, see previous section.

Knowing the experimental plasma power and substituting the estimated plasma temperature, based on eq. 5, as T_2 in eq. 6, we can estimate the mass flow rate passing through the plasma. Then using this estimated plasma mass flow rate and the equilibrium NO concentration, we can calculate the mass flow rate of NO in the plasma. Finally, knowing the plasma mass flow rate of NO, we can calculate the total mass flow rate in which the NO concentration is equal to the experimental values. If this calculated total flow rate is roughly the same as the total experimental mass flow rate fed to the reactor, the assumption of an equilibrium plasma is valid. Therefore, we can assume that the gas flow surrounding the plasma is mixed with the mass flow passing through the plasma and quenches the back-reactions, hence preserving the plasma-produced NO.

As mentioned earlier, our model is developed based on thermodynamic equilibrium considerations, indicating that we consider our system to be a thermal plasma. Thermal plasmas, in general, operate at high temperatures, and exhibit equilibrium dynamics [2]. These two unique characteristics highlight the need to account for reversible reactions when dealing with the kinetic mechanisms. For these reasons we chose forward rate coefficients based on critically evaluated data gathered for combustion research. Because these rate coefficients are reported with high accuracy and because these are elementary reactions, detailed balancing can be applied to determine the rate coefficients for the back-reactions. In fact, we are not directly interested in the kinetics of the process, but rather in the thermodynamics, which means that no matter what forward rate coefficient we use, if the backward rate coefficient is calculated based on the detailed balance principle, we will reach the correct thermodynamic equilibrium concentrations. Nevertheless, we have still chosen the most accurate rate coefficients we could find, which ensures that the reverse rate coefficients have the same level of accuracy. As a result, in our reaction scheme, we have considered four reversible chemical reactions, as presented in Table 1, and we used the detailed balance principle to calculate the rate coefficients of the reverse reactions.

Table 1. Chemical reactions considered in the model

	Reaction*	Rate coefficient forward reaction [m^3/s]	Ref.
(1)	$N_2 + M \leftrightarrows N + N + M$	$5 \times 10^{-8}\left(\frac{-133200}{T}\right) \times \left(1 - \exp\left(\frac{-3354}{T}\right)\right)$	[42]
(2)	$O_2 + M \leftrightarrows O + O + M$	$3.7 \times 10^{-8}\exp\left(\frac{-59380}{T}\right) \times \left(1 - \exp\left(\frac{-2240}{T}\right)\right)$	[42]
(3)	$N_2 + O \leftrightarrows NO + N$	$9.7 \times 10^{-21} \times T^{1.01} \times \exp\left(\frac{-3120}{T}\right)$	[43]
(4)	$O_2 + N \leftrightarrows NO + O$	$3 \times 10^{-16} \times \exp\left(\frac{-38000}{T}\right)$	[43]

* M is any molecule in the gas.

The temperature-dependent enthalpy of the considered species, used to calculate the heat capacity, is taken from the NASA Glenn polynomials [44]. The model was used to calculate the equilibrium NO concentration as a function of temperature, as well as the heat capacity of the mixture as a function of temperature, used to calculate the energy needed to heat the gas to a certain temperature, from which the EC is obtained to reach the equilibrium NO concentration at a certain temperature:

$$\mathrm{EC}\left[\frac{MJ}{mol}\right] = \frac{q\left[\frac{J}{Kg}\right] \times 29 \times 10^{-3}\left[\frac{kg}{mol}\right]}{x_{NO}} \times 10^{-6}\left[\frac{MJ}{J}\right] \quad (7)$$

Where x_{NO} is the mole fraction of NO calculated by the model.

4. Results and discussion

As mentioned above, we investigated the performance of the two different plasma reactors, to obtain more insights in the effects of upscaling. Due to the clearly different range in flow rates of the small and large reactor, while using the same PSU (see above), both reactors operate in a different SEI range. The small reactor operates in a pin-to-pin configuration with axial flow going through the plasma region. By using a current-controlled PSU, we varied the current between 200 – 500 mA, for flow rates of 5, 10, 15 and 20 ln/min. In addition, we investigated the effect of the interelectrode spacing, by varying the distance between the electrodes between 7 and 14 cm. This configuration covers the high SEI range, with maximum value of 7.6 kJ/l.

To investigate the potential of scaling up plasma-based NF, we developed a larger version of this reactor, which can operate both in pin-to-pin and torch configuration. The latter configuration is put forward as a solution to overcome the limitations of the pin-to-pin configuration, as explained below. The large reactor is operated by the same PSU, but the current range could be extended from 300 to 1000 mA, with flow rates

of 100, 200 and 300 ln/min. As explained above, this yields a lower SEI range, because the PSU could not supply higher current. In addition, the distance between the electrodes was also varied between 7 and 14 cm in the pin-to-pin configuration.

Last but not least, in order to aid the analysis of our experimental results and obtain more insight in the effects of upscaling, we performed calculations based on thermodynamic equilibrium considerations. For all of the conditions, we are reporting the total NO_x concentration (being $NO+NO_2$).

4.1. Small reactor

The plasma in the small reactor could not be sustained in the full current range between 200 and 500 mA for all gas flow rates; see Figure 4, which depicts the plasma power as a function of current. More specifically, we observed two regimes of plasma operation as a function of flow rate, as presented by the photographs in figure 5. With increasing gas flow rate, the discharge transitions from a stable and rather diffuse column (Figure 5, 5 ln/min) to a more contracted and oscillating column (Figure 5, 20 ln/min), which reduces the stability at low currents. The blue region in Figure 5 is the current-conducting region of the discharge, while the orange glow observed around the core is the NO_2 emission, as also observed by Machala et al. [45]. Furthermore, upon increasing current, the plasma starts gliding along the exposed part of the electrode, leading to a longer discharge, not corresponding to the exact distance between the electrodes. We note that despite the plasma was stable for 5 ln/min, the voltage and current as a function of time were oscillating around the mean voltage and current values (Figure S3.a). Furthermore, there is a bright contracted spot on the cathode, indicating the plasma operates in the arc regime.

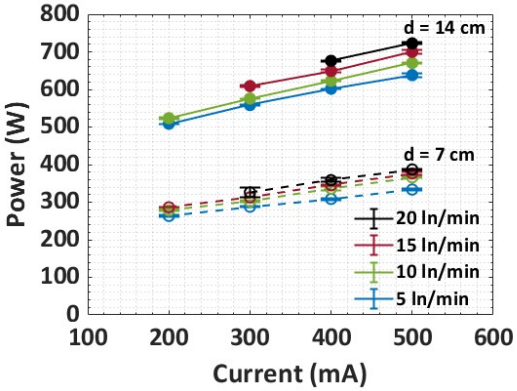

Figure 4. Plasma power as function of applied current, for the four different flow rates and two different distances between the electrodes (dashed lines/open symbols, and solid lines/closed symbols, for d = 7 and 14 cm, respectively). Error bars are indicated by the horizontal lines; the actual values are too small to be visible.

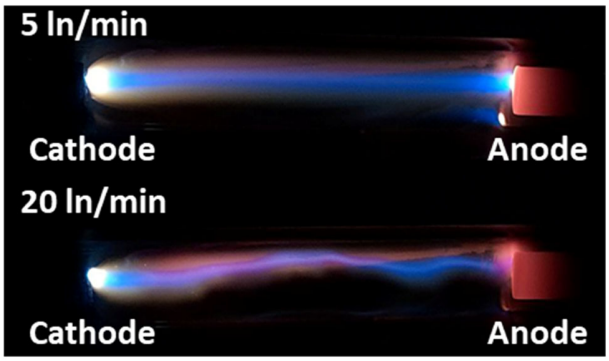

Figure 5. Transition of plasma regime upon increasing feed gas flow rate, from a stable and diffuse column at 5 ln/min, to a contracted and oscillating column at 20 ln/min. Both images are taken at the same current of 500 mA.

As mentioned, figure 4 illustrates the plasma power as a function of applied current, for the four different flow rates and two different distances between the electrodes. The plasma power linearly rises with current for both 14 and 7 cm, and for all flow rates. This trend is natural for plasma sustained between two opposing electrodes [45]. As the gas flow rate increases, we observe an increase in plasma power, due to the enhanced convective losses. Indeed, the plasma becomes more resistive, and a higher voltage is required to sustain the discharge at the same current. For example, we can see a 53 W increase in power between 5 and 20 ln/min for 500 mA and 7 cm distance between the electrodes. This behavior is consistent with the modelling of a similar type of discharge in N_2 in our previous work [46].

When the distance between the electrodes increases from 7 to 14 cm, the gas flow rate has a stronger effect on the voltage required to sustain the discharge, because of the enhanced interaction between plasma and gas flow. As a result, there is a larger increase in power for 14 cm distance between 5 and 20 ln/min flow rates, e.g., for 500 mA, the difference is 85 W. As the distance between the electrodes increases, we expect the power to rise with the same factor. Indeed, in Figure 4, we do observe a rise in power by nearly a factor of two for all investigated conditions. For 5 ln/min, the rise in power between 7 and 14 cm is roughly 1.91 for all currents, while for 20 ln/min it is 1.87.

The measured NO_x concentration as function of current, for the different flow rates and distances between the electrodes is presented in Figure 6. For all conditions we observe a rise in NO_x concentration as a function of current and distance between the electrodes and a drop as a function of flow rate. The highest NO_x concentration is 3.51%, for a current of 500 mA, a flow rate of 5 ln/min and distance between the electrodes of 14 cm. For 7 cm distance between the electrodes, despite the linear behavior in power as a function of current (Figure 4), we see a nonlinear behavior in the NO_x concentration for 10 and 15 ln/min

(Figure 6 a), while for 5 and 20 ln/min we do observe a nearly linear relationship. For 14 cm distance (Figure 6 b) a nonlinear rise in NO_x concentration is observed only for 10 ln/min, while the other flow rates yield a nearly linear trend.

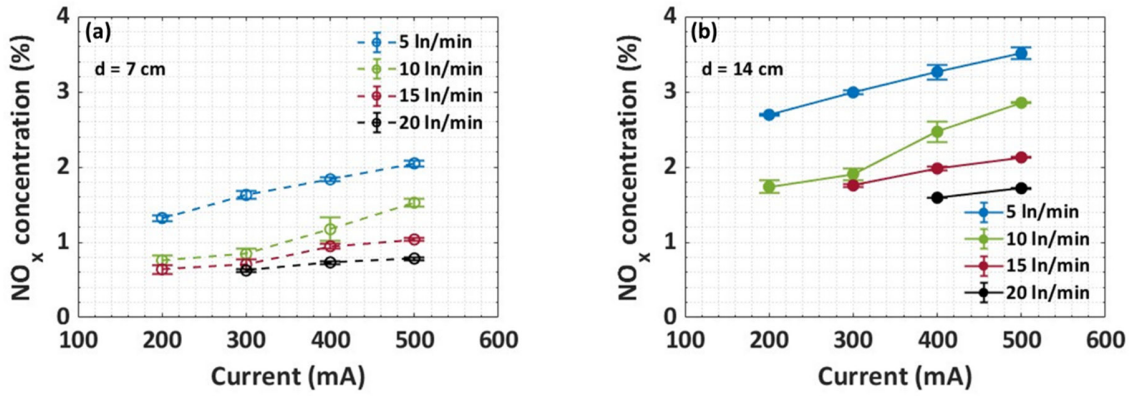

Figure 6. Total NO_x concentration as function of current, at different flow rates, for (a) 7 cm and (b) 14 cm, in the small reactor. Error bars are indicated but are often too small to be visible.

Doubling the distance between electrodes does not result in the same rise in NO_x concentration, despite the nearly linear relationship for power (Figure 4). For example, at 500 mA, the ratio of the NO_x concentration between 7 and 14 cm is 1.71 for 5 ln/min and 2.19 for 20 ln/min. This shows that increasing the distance between the electrodes, and thus the length of the plasma, is a crucial parameter. The result is most striking at 20 ln/min, where the rise in power was only 1.87. For the larger electrode distance, the relative increase in NO_x concentration is thus higher than the relative increase in power, and as a result, the process is overall improved in terms of EC (see figure 7).

Indeed, in order to more clearly present the relationship between power and produced NO_x concentration, we plot in Figure 7 the results for both EC and NO_x concentration as a function of SEI, for the different flow rates and distances between the electrodes. As mentioned before, the SEI is the ratio of power over flow rate (eq. 2), and it is an important parameter to determine the reactor performance. We clearly see a drop in the EC and a rise in the NO_x concentration as function of SEI in the entire SEI range. This indicates that the performance, both in terms of NO_x concentration and EC, would further improve upon higher SEI. We will investigate this in future work, when we have a PSU that can produce higher power.

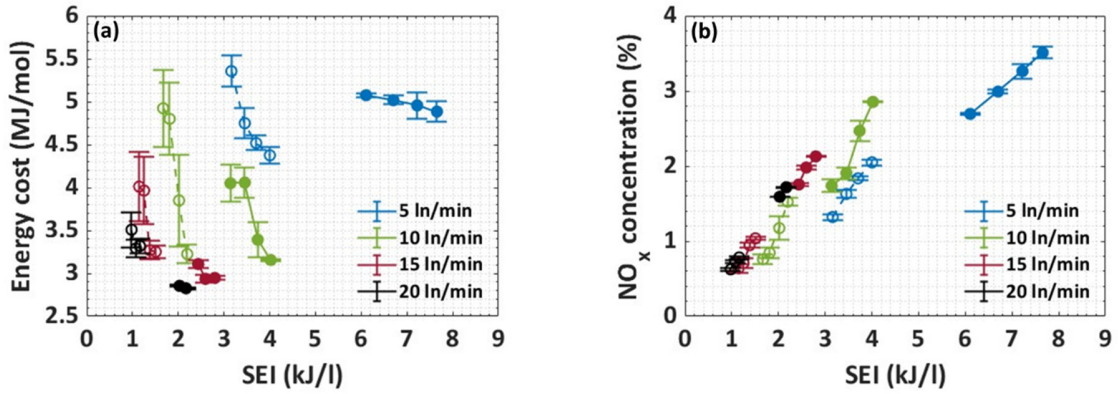

Figure 7. EC (a) and NO_x concentration (b) as a function of SEI, for the four different flow rates and a distance between the electrodes of 7 and 14 cm (dashed lines/open symbols, and solid lines/closed symbols, respectively). Error bars are indicated but are sometimes too small to be visible.

Interestingly, the EC as a function of SEI strongly depends on the gas flow rate, showing an additional decreasing relationship at higher flow rates. Indeed, the SEI is defined by power and flow rate. The power rises a bit with flow rate, but not proportionally. Hence, the SEI clearly drops with rising flow rate. The NO_x concentration also drops with rising flow rate (Figure 6), but less strongly than the drop in SEI. As the EC is determined by both NO_x concentration and SEI, we obtained the lowest EC at the highest flow rate, i.e., 2.8 MJ/mol, for an SEI of 2.1 kJ/l (Figure 7 a). However, this condition corresponds to a NO_x concentration of only 1.72% (Figure 7 b). On the other hand, the highest NO_x concentration of 3.51% (obtained at 5 ln/min, 14 cm and highest SEI of 7.6 kJ/l; Figure 7 b) yields an EC of 4.8 MJ/mol (Figure 7 a).

Because of the relationship between power, flow rate and NO_x concentration, we achieved multiple points with similar SEI but clearly different EC (cf. Figure 7 a). This effect was also observed by Pei et al., who also investigated the EC and NO_x concentration as a function of distance between the electrodes for a DC glow discharge [36]. This relationship shows that the distance between electrodes provides an additional degree of freedom.

It should be realized that all these values are obtained for NO_x production simply from air (N_2:O_2 = 80:20). Care should be taken when comparing the results with literature (cf. Figure 1 in the introduction), where the best results are typically reported for oxygen-enriched air (usually N_2:O_2 = 50:50) (e.g., [25–27]). However, we want to design an industrial process, where starting from air is more convenient, and otherwise the cost of producing oxygen-enriched air should also be accounted for, which is never done in literature.

4.2. Large reactor in pin-to-pin configuration

For the large reactor in the pin-to-pin configuration, the plasma could be sustained in the current range of 400 - 1000 mA when the swirling flow was applied. Without swirling flow, the plasma was highly unstable, and we could only operate at higher currents. Hence, we discuss here only the results with swirling flow, and we refer to SI (Section 5, Figure S5) for the results without swirling flow.

The power as a function of current for different flow rates and distances between the electrodes in the large reactor in pin-to-pin configuration are presented in Figure 8.

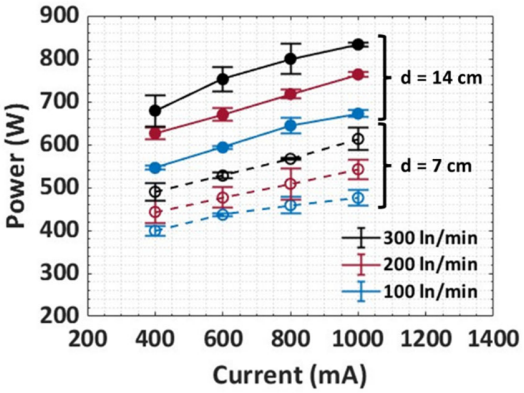

Figure 8. Plasma power as a function of current, for three different flow rates and two distances between the electrodes (dashed lines/open symbols and solid lines/closed symbols, for d = 7 and 14 cm, respectively), in the large reactor in pin-to-pin configuration. Error bars are indicated but are sometimes too small to be visible.

Similar to the observations in the small reactor, we can see a linear increase in power as function of current for all investigated conditions. Again, the deposited power increases with flow rate and with interelectrode distance. Increasing the distance between electrodes by a factor two yields a rise in power by much less than a factor two for the same current and flow rate. For example, for 1000 mA and 300 ln/min, the ratio in power between 14 and 7 cm is 1.35. This is far less than what we observed in the smaller reactor, where the power almost doubled.

The NO_x concentration as a function of current, for different flow rates and for a distance between the electrodes of 7 and 14 cm, is presented in Figure 9. We again see that the NO_x concentration decreases with flow rate and increases with current and distance between electrodes. There is a nearly linear increase as a function of current, although with a relatively shallow slope. As the rise in NO_x concentration as a function of current is very similar for all flow rates, the drop in NO_x concentration as a function of flow rate is nearly constant across the entire current range.

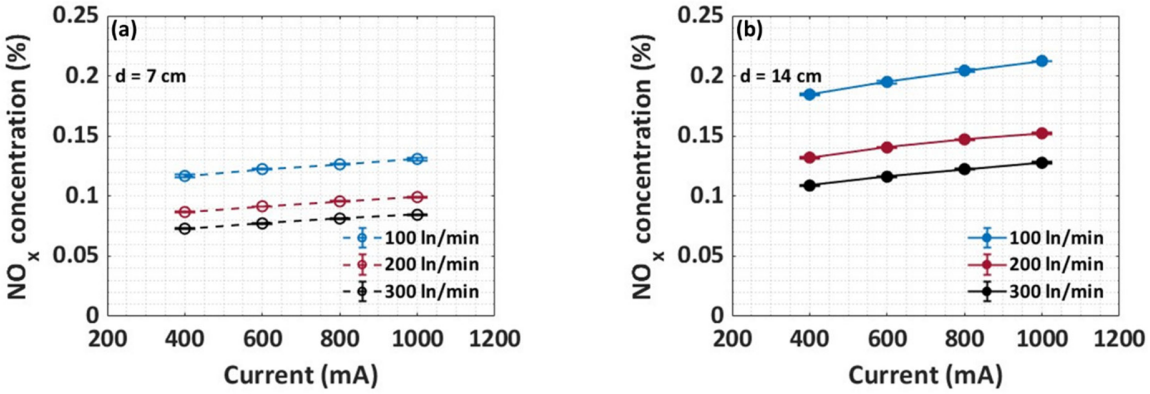

Figure 9. NO_x concentration as a function of current, for three different flow rates and a distance between the electrodes of (a) 7 cm, and (b) 14 cm, in the large reactor in pin-to-pin configuration. Error bars are indicated but are too small to be visible.

The highest NO_x concentration obtained is 0.21%, for a distance between the electrodes of 14 cm, a current of 1000 mA and a flow rate of 100 ln/min. Because of the significant reduction in SEI range, as compared to the small reactor, the NO_x concentration is significantly lower for all investigated conditions compared to the small reactor, where values up to 3.51% were obtained (Figure 6 b). We can see that the relative NO_x increase, upon rising distance between the electrodes, is again higher than the increase in power, e.g., it is 1.51 for 1000 mA and 300 ln/min, while the relative rise in power was only 1.35 (Figure 8). Still, the relative increase is smaller than twice. However, as the rise in NO_x concentration is larger than the rise in power, the EC will drop upon increasing distance between the electrodes. The EC and NO_x concentration as a function of SEI for different flow rates and distances between the electrodes are presented in Figure 10.

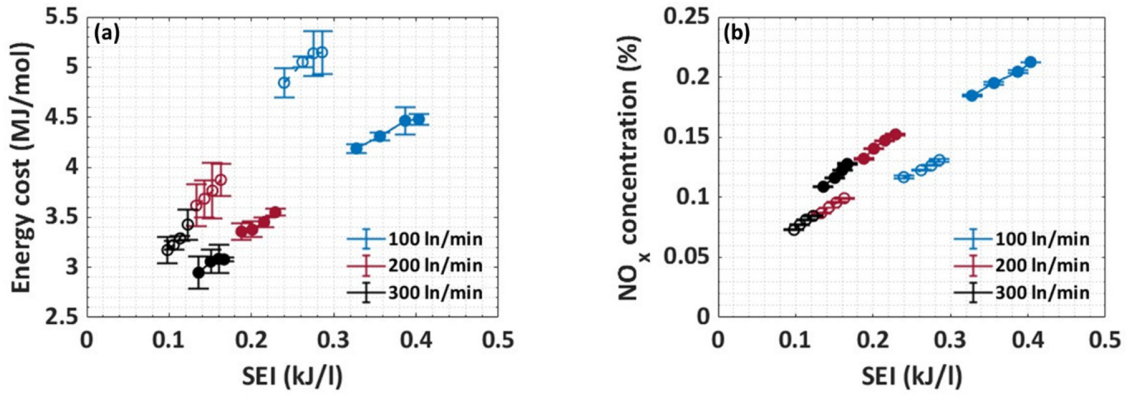

Figure 10. EC (a) and NO_x concentration (b) as a function of SEI, for three different flow rates and two distances between the electrodes (dashed lines/open symbols, and solid lines/closed symbols, for d = 7 and 14 cm, respectively), in the large reactor in pin-to-pin configuration. Error bars are indicated but are sometimes too small to be visible.

In contrast to the small reactor, here the EC increases, instead of decreases with SEI. The reason will be explained by our modeling insights in section 4.5 below. Again, for the same SEI, we observe a lower EC at 14 cm distance between the electrodes, because the NO_x concentration rises faster with interelectrode distance than the power (cf. same behavior for the small reactor in Figure 7a). The EC reaches its lowest value at an SEI of 0.13 kJ/l, for 300 ln/min and 400 mA, and is equal to 2.9 MJ/mol. It corresponds however to a low NO_x concentration of only 0.11%. The NO_x concentration increases nearly linearly as a function of SEI, and again, for the same SEI condition we reach a much higher NO_x concentration at larger distance between the electrodes. As mentioned above, the highest NO_x concentration obtained is 0.21%, at 14 cm distance, 100 ln/min and SEI of 0.4 kJ/l, but it corresponds to a fairly high EC of 4.5 MJ/mol. Based on these results, it is clear that even if we reduce the SEI significantly, the EC will not improve, because the NO_x concentration will also drop (cf. Figure 10 b).

We believe that the relationship between NO_x concentration and SEI inside the plasma is the driving force for reducing the EC, rather than the overall SEI. However, in the formulas, the overall SEI is always used. The SEI inside the plasma is (considerably) higher than the overall SEI, which is attributed to the limited flow going through the plasma, due to the plasma confinement, i.e., the plasma does not fill the entire reactor. This is most obvious in the large reactor. Note that the SEI inside the plasma is not a macroscopic parameter, although it is the intrinsic parameter affecting the performance. A clarification of this process is given in the next section.

Comparing Figure 7 a and Figure 10 a, we observe an opposite trend for the EC as a function of SEI in the small and large reactor in pin-to-pin configuration. According to equation 3, the EC increases upon increasing SEI, and decreases upon increasing NO_x concentration. In the small reactor, the rise in NO_x concentration with SEI is, proportionally, higher than the rise in power, and thus, the EC drops with increasing SEI. In contrast, in the large reactor, the power rises more with SEI than the NO_x concentration, and therefore, the EC increases with SEI. This explains the different behavior for the small and large reactor. We believe the reason for this different behavior is the lack of sufficient mixing between the cold gas and the hot plasma afterglow in the large reactor. The cold gas should quench the back-reactions, thus leading to higher NO_x production, but in the large reactor, due to the reactor design or the flow pattern, this is not happening as efficiently as in the small reactor. We will address this limitation in our future studies.

Finally, the NO_x concentration and EC as a function of SEI without swirling flow are presented in the SI (section 5, Figure S5). The highest NO_x concentration is 0.25%, obtained at the highest SEI, and corresponds to an EC of 4.8 MJ/mol. A lower EC of 3.3 MJ/mol was obtained at a lower SEI of 0.26 kJ/l, but the corresponding NO_x concentration was only 0.19%. Hence, when compared to the reactor with

swirling flow, the NO_x concentrations are slightly higher, but the EC is somewhat worse. This indicates that the swirling flow not only helps to improve the plasma stability, but also the reactor performance in terms of EC.

4.3. Large reactor in torch configuration

From previous section it is clear that the large reactor in pin-to-pin configuration is not very successful, due to the contracted nature of the plasma arc, limiting the amount of gas flowing through the plasma. This will be discussed in more detail below. To solve this limitation, we also tested the large reactor in torch configuration with the same swirling flow pattern. In the torch configuration, the bottom electrode of the reactor was removed, and the plasma was free to glide and rotate within the reactor, thus occupying a somewhat larger volume in the reactor (longer plasma column). For the torch configuration, the plasma was also stable in the current range of 400 to 1000 mA. The power and NO_x concentration as a function of current for three different flow rates are presented in Figure 11.

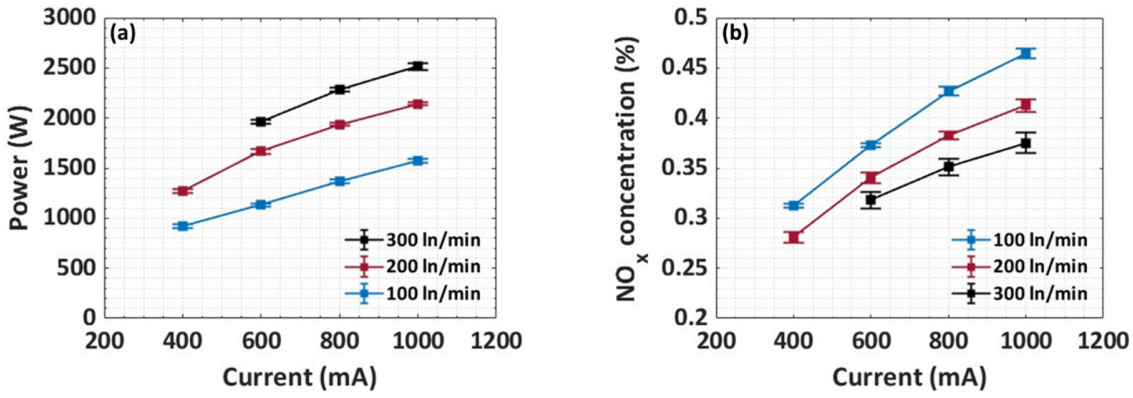

Figure 11. Power (a) and NO_x concentration (b) as a function of current, for three different flow rates in the large reactor in torch configuration. Error bars are indicated but are mostly too small to be visible.

We can again see a nearly linear relationship between the current and power (Figure 11 a). The power again increases with flow rate, reaching the highest value achieved in this study, i.e., 2500 W for 300 ln/min and 1000 mA. Indeed, because the plasma can freely glide and rotate within the reactor body, the plasma column is longer and a higher voltage drop can be achieved, which results in a higher power deposited in the reactor. As a result, there is also a significant increase in the NO_x concentration compared to the pin-to-pin configuration (Figure 11 b). The NO_x concentration also shows a nearly linear dependence as a function of current. The highest NO_x concentration measured in this configuration was for 100 ln/min and 1000 mA and is equal to 0.46%. The NO_x concentration again decreases with rising flow rate but does not drop below 0.28%. Because higher power is deposited in this configuration, the SEI is also higher.

The EC and NO_x concentration as a function of SEI are presented in Figure 12. Similar to the pin-to-pin configuration, the EC increases with SEI. The lowest EC is achieved at 0.4 kJ/l, reaching 2.9 MJ/mol, corresponding to a NO_x concentration of 0.32%. The EC that corresponds with the highest NO_x concentration (of 0.46%) is 4.8 MJ/mol. Compared to the large reactor in pin-to-pin configuration, the EC is the same, but the NO_x concentration is more than double (e.g., highest NO_x concentration of 0.46% vs. 0.21% in torch vs. pin-to-pin configuration). Hence, overall, the torch configuration yields a better performance, due to the longer plasma column. Compared with the small reactor, the EC is slightly higher (2.9 vs. 2.8 MJ/mol), but the NO_x concentration is still dramatically lower (maximum 0.45% vs. 3.5%). This shows how reactor upscaling is quite challenging, and that reactor design is crucial for achieving a scaled-up process with high NO_x concentrations and low EC.

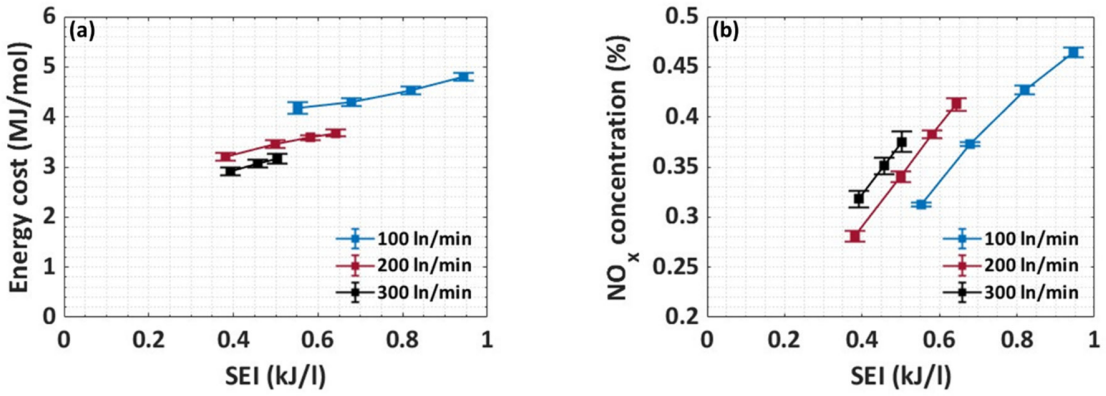

Figure 12. EC (a) and NO_x concentration (b) as function of SEI, for the large reactor in torch configuration. Error bars are indicated, but are mostly too small to be visible

4.4. Comparison of production rate in the three reactors

In reactor upscaling, the production rate (PR) becomes a very important parameter, indicating whether reducing the SEI by increasing the gas flow rate through the reactor has a substantial effect, or only dilutes the products produced by the plasma. To determine whether the scaling up is successful, we evaluated how the PR changes as a function of SEI, for the conditions of lowest EC, for the three reactors, i.e., the small pin-to-pin, large pin-to-pin and large reactor in torch configuration; see Figure 13.

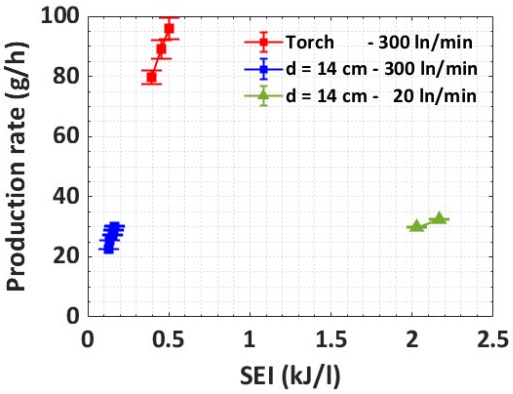

Figure 13. Total NO_x production rate as a function of SEI, for the three different reactors, i.e., small pin-to-pin, large pin-to-pin, and the large reactor in torch configuration. The conditions with the lowest EC are presented here.

It is logical that the PR increases with increasing SEI. The PR trends closely follow the trends in NO_x concentration. When comparing both reactors in pin-to-pin configuration, we see that they yield more or less the same PR (in the range of 20 – 35 g/h). Indeed, the large reactor operates at 15 times higher flow rate, but the obtained NO_x concentration is about 15 times lower (maximum 3.51% vs. 0.21% in the small vs. large reactor). Both effects compensate each other when determining the PR. The corresponding EC in the large reactor is however slightly lower (4.5 vs. 4.9 MJ/mol in the large vs. small reactor), due to the much lower SEI (linked to the much higher flow rates).

These results are very important, as they indicate that the mass flow heated to the temperature leading to NF (or in other words, the amount of gas flowing through the plasma arc) is nearly the same for the large and small reactor, despite the substantially higher flow rate passing through the large reactor. This suggests that the plasma arc in the large reactor is very contracted and is probably not wider than the plasma arc in the small reactor, despite the much larger reactor dimensions. Hence, this limits the amount of gas flowing through the plasma.

In general, we can conclude that the large reactor in pin-to-pin configuration is not very successful for upscaling, at least in this configuration, because the PR is not enhanced. The reason for the latter is the low NO_x concentration obtained, due to the higher flow rates, which dilute the NO_x produced in the plasma, while the amount of NO_x produced in the plasma, determined by the flow passing through the plasma arc, is the same for the small and large reactor, due to the similar plasma arc diameter, which results in the same volume of gas passing through the plasma, as explained above.

The question arises whether this limitation could be mitigated if the PSU of the large reactor could deliver much higher power, leading to much higher SEI. The answer is no, because, even if the PSU would deliver

much higher power, the arc diameter would not rise with the same extent, so there would still be gas not flowing through the arc, causing dilution of the produced NO_x.

In summary, our results indicate that the NO_x production inside the plasma is very similar for the small and the large reactor, but due to the additional (much higher) flow rate in the large reactor, which is not passing through the plasma (and thus not giving rise to NO_x production), the overall NO_x production in the large reactor is lower. This effect will be discussed in more detail in the next section, by means of thermodynamics equilibrium calculations. Nevertheless, despite the lower NO_x concentration in the large reactor, the EC is very similar as in the small reactor, due to the lower SEI.

From comparing the NO_x concentrations in the small and large reactor in pin-to-pin configuration, clearly, we need other modifications to the reactor design in order to increase the performance, and to overcome the fundamental limitation of the limited amount of gas passing through the arc, which causes dilution of the NO_x produced by the plasma.

Treatment of only a limited fraction of the feed gas by the plasma is one of the main limitations of plasma-based gas conversion, resulting in low NO_x concentrations. The reactor configuration and gas flow pattern can significantly affect the amount of gas passing through the plasma, due to the geometrical configuration of the arc, which is typically concentrated in the center of the reactor. Figure 13 illustrates that, in our case, this limitation can, to some extent, be overcome by operating the large reactor in torch configuration. As mentioned earlier, the large reactor in torch configuration is the same as the large reactor in pin-to-pin configuration, but with bottom electrode removed and reactor body acting as the ground electrode. In this configuration, the plasma (arc) can freely glide inside the reactor, and its geometry will be different from just a pseudo-cylindrical column in the center between two opposing electrodes. Indeed, the generated plasma will be somewhat larger than the plasma column in the pin-to-pin configuration, and thus, the delivered power to the reactor will be deposited to a larger fraction of the gas feed. In other words, a larger amount of gas is treated by plasma, and therefore, the obtained NO_x concentration, and thus also the PR, can be improved. Indeed, our results, for the large reactor in torch configuration, show more than three times higher PR, while sustaining the EC below 3 MJ/mol. The highest PR that we achieved is 96 g/h, for an SEI of 0.5 kJ/l, while at 0.4 kJ/l (corresponding to the lowest EC of 2.9 MJ/mol), the PR is 80 g/h. The reason for these good results can thus be attributed to the fact that, in the torch configuration, the NO_x concentration is much higher than in the pin-to-pin configuration, for nearly the same EC, due to the larger plasma column, which occupies a larger fraction of the reactor volume, thus increasing the amount of gas treated by the plasma. The latter enhances the thermal efficiency of the system and shows promise for upscaling purposes. Hence, we can conclude that when paying sufficient attention to the reactor design,

substantial improvements in the flow pattern and power deposition mechanisms are feasible, and therefore, a successful scale up can be reached.

An important aspect in terms of upscaling is the question of long-term operation of plasma reactors. In general, erosion of the electrodes, and of the reactor, is one of the limitations for long-term operation. This is one of the reasons why so-called 3D GA plasma reactors were introduced as an alternative to classical 2D GA reactors[47]. In the design of our large reactor, the main components, including the electrodes and the main reactor body, are made from temperature- and corrosion-resistant materials. This greatly increases the reactor lifetime, thereby enabling long-term process operation.

As mentioned in the Introduction, except for the Birkeland-Eyde (BE) process, to our knowledge, all other reported NF plasma processes were operated in lab scale reactors. Hence, the question arises how our upscaled reactor differs from the BE process. In the BE process, magnetic fields had to be used to stabilize the plasma, while we are using a swirling flow to achieve the same effect. In this way, we avoid the costly operation of large electromagnets, and at the same time we are able to reach the very low EC necessary for the industrial implementation of this technology. The BE process further utilized high current alternating current (AC) arcs, which created an asymmetric heating profile within the gas flow. In our reactors the gas is heated more uniformly through DC current, which allows for better control of the gas flow dynamics[6,7].

4.5. Local Thermodynamic equilibrium (LTE) calculations to explain the experimental observations

In earlier work from our group on plasma-based NF, the non-thermal Zeldovich mechanism was reported to be important (e.g., [refs]). However, new insights have revealed that in quasi-thermal plasmas, the thermal mechanism dominates, as the vibrationally excited levels are not overpopulated with respect to the Boltzmann distribution at the gas temperature. In other words, there is no vibrational-translational non-equilibrium. Therefore, we can safely use LTE calculations to gain insights into the process. Indeed, previous research conducted by Naidis et al. has shown that arcs sustained by currents larger than 200 mA are in LTE [40]. The calculated NO concentration and corresponding EC for producing this NO, from air, as a function of temperature, assuming LTE, are presented in Figure 14.

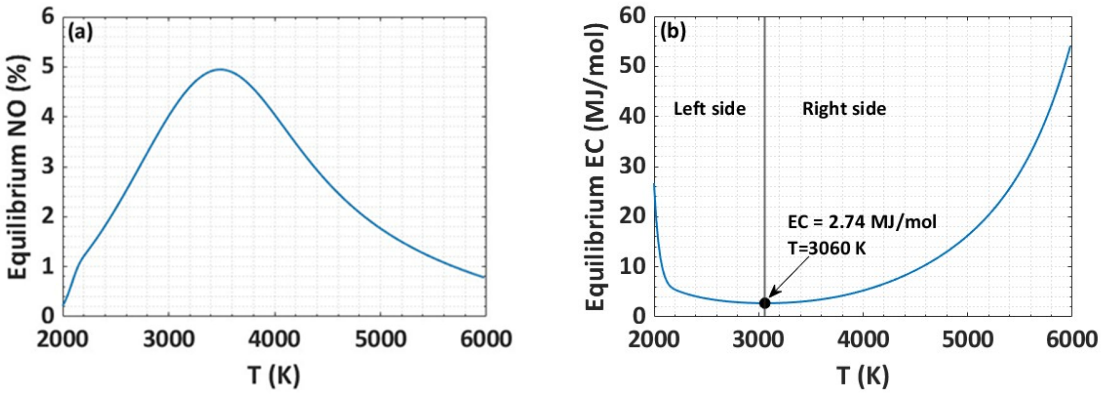

Figure 14. Calculated NO concentration (a) and EC (b) as a function of temperature, assuming LTE.

We can see that in the lower temperature region (< 3500 K), there is a steep increase in NO concentration as a function of temperature, which reaches a maximum of 5 % at 3500 K. The maximum is followed by a clear drop at higher temperatures, reaching below 1 % above 6000 K (see Figure 14 a). This indicates that for relatively small changes in temperature, a large increase in NO concentration will be observed in the temperature range of 1900 – 3200 K. The lowest EC calculated is 2.74 MJ/mol, for a temperature of 3060 K. Note that this value is very close to the lowest EC of 2.8 MJ/mol that we obtained experimentally in the small reactor for 20 ln/min and an SEI of 2.1 kJ/l (figure 7 a). Also in the large reactor, we achieved similar values (i.e., 2.9 MJ/mol, again close to the thermodynamic limit) in the pin-to-pin and torch configuration for 300 ln/min and SEI values of 0.13 (figure 10 a) and 0.4 kJ/l (figure 12 a), respectively. The EC decreases gradually in the temperature range of 2000 – 3000 K, leading to this minimum value, after which it starts rising (Figure 14 b). These calculations present the thermodynamic limit of the EC, together with the maximum concentration of NO that can be obtained for this EC, being 4.2 % (see Figure 14 a). We will now use this information to obtain more insights in our experimental results. The power delivered to the reactor can either be deposited in the total gas flow rate fed to the system, or it can be deposited in a limited fraction of the gas stream passing through the plasma. The latter suggests that the plasma (arc) is contracted, and the gas flow surrounding the plasma (with much higher flow rate) can intermix with the plasma-treated gas and preserve the NO_x produced by the plasma, through quenching of the back-reactions. Therefore, in section 4.6, we first assume that the power is deposited in the total gas flow fed to the reactor, and knowing the experimental plasma power, we calculate the average gas temperature in our reactor using eq. 6, aiming to investigate whether this assumption is valid or not.

4.6. Calculated gas temperature in the reactors

The average gas temperature, calculated as explained in previous section, is plotted in Figure 15 as a function of current for different flow rates, for the high SEI region and low SEI region, corresponding to the small (a) and large (b) reactor, respectively.

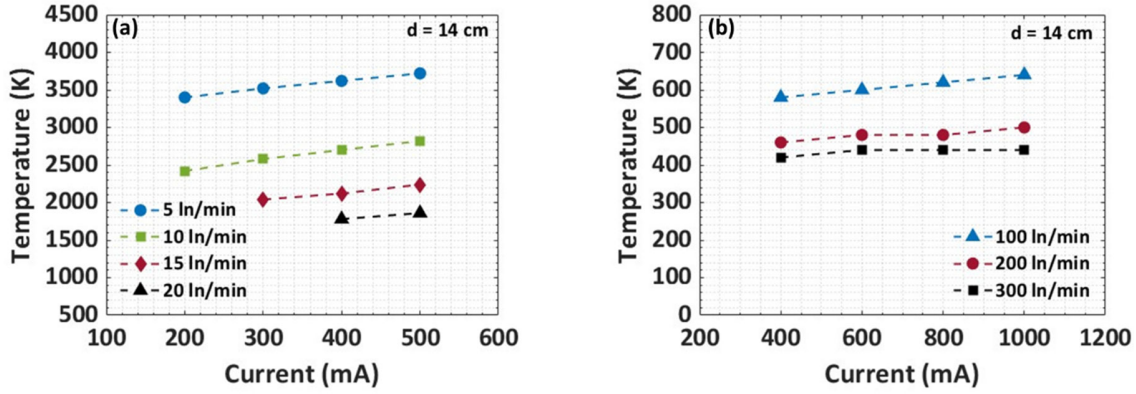

Figure 15. Average gas temperature, calculated from the measured power and flow rate, using eq. 6, in the small reactor (a) and large reactor (b).

In the small reactor (Figure 15 a), the average temperature increases linearly with current, although the slope is shallow, reaching its highest value of 3720 K for 500 mA and 5 ln/min. The gas temperature drops as a function of the gas flow rate, reaching values below 2000 K for 20 ln/min. Based on these calculations for the small reactor, we should be able to achieve very efficient NO_x production at 200 mA and 5 ln/min, or at 500 mA and 10 ln/min. In reality, we observe much lower NO_x concentration compared to the equilibrium calculations, i.e., maximum 3.5. This observed discrepancy can be attributed to the back-reactions taking place in the afterglow of the plasma, i.e., the recombination of NO with O or N atoms, back into O_2 or N_2 molecules (see reverse reactions 3 and 4 from Table 1) [26]. As a result, we measure lower NO_x values than theoretically predicted based on thermodynamic equilibrium. Furthermore, we can see that for the higher flow rate, the average gas temperature presented in Figure 15 a will yield far less NO, according to the thermodynamic equilibrium calculations (cf. Figure 14 a), than what we measure in our small reactor, indicating that we are producing more than the equilibrium, especially for the case with the lowest EC of 2.8 MJ/mol where the NO_x concentration was 1.8%.

Even more interesting is that in the large reactor (Figure 15 b), the temperatures are consistently below 700 K, which creates conditions impossible for NO_x production, simply based on thermodynamic equilibrium. Hence, the temperatures plotted in Figure 15 b are unrealistically low for this reactor, at least for the plasma core. Because the power increases proportionally with the flow rate and the flow rate is significantly larger,

a very small difference in temperature is observed between 200 and 300 ln/min. This means that the temperature should be based on the fact that all of the energy input is focused not on the total reactant but only a portion of the reactant resulting in much higher temperature than used in the equilibrium analysis. Because of that, comparison of the composition and EC of the product is not fair to be compared to the condition where the SEI is calculated based on the condition for the energy supply for all of the reactant. More realistic temperatures will be presented in section 4.7 below. The reason for the observed discrepancies in the large reactor, and also for the high flow rates of the small reactor, lies in the contracted nature of the plasma, for which the above method of calculating the average gas temperature (based on experimental plasma power and gas flow rate) breaks down. Atmospheric pressure plasmas indeed experience a contracted power density profile, due to the non-linear relation between gas heating and the electric field [39]. In order to calculate the SEI and the average temperature, we assumed that the power is deposited uniformly in the reactor volume and the entire flow passes through the chemically active plasma region. Obviously, this gives rise to such unrealistically low plasma temperatures, and invalidates the assumptions of power deposition in the total gas flow rate passing through the reactor. Indeed, experimentally, the measured plasma power is deposited in a very small volume and only a fraction of the gas flow is heated to the (much higher) temperatures responsible for NO_x production.

As a result, we usually observe an inverse relationship between EC and NO_x concentration, meaning that they both rise as a function of SEI (see Figure 10 and 12 above). This is a sign that at high SEI (and thus higher NO_x concentrations), the back-reactions become dominant, and the EC increases considerably. When the (macroscopic) SEI is lower, and because the plasma arc is not filling the entire reactor width, the cold gas surrounding the plasma quickly mixes with the exhaust, stopping the back-reactions and diluting the products, resulting in a more efficient process, but at the price of lower NO_x concentrations. In this situation, the SEI inside the plasma is high, given that a very small amount of the mass flow is in a plasma state and all the power is deposited in this very small volume, while on the other hand, the macroscopic SEI (of the total reactor) is low, because of the large averaging.

4.7. Improved thermodynamic equilibrium calculations

Our calculation results in section 4.6 invalidated the assumption of power deposition in the total reactor volume, for high gas flow rates, and suggested that the delivered power is only deposited in a limited fraction of the gas stream fed to the reactor. In order to account for these effects, we modified the equilibrium calculation of the gas temperature by making two strong assumptions. First, we assume that the plasma is thermally insulated, and non-equilibrium effects are negligible. This assumption is valid because the plasma system under study exhibits characteristics of thermal plasmas, and therefore, non-equilibrium effects are not important in such a system. Additionally, since the delivered power is deposited

in a small fraction of the gas, we can assume that the cold gas surrounding the plasma stops the back-reactions through mixing, and all the products generated in the hot region are recovered. Following these assumptions, we can correlate the experimentally measured EC with the theoretically calculated EC, and this allows us to correctly determine the temperature inside the plasma. Using eq. 6 and the experimental plasma power, we can then determine the gas flow passing through the hot region, for the temperature determined by the EC.

Based on Figure 14 b, we can see that for the same EC we can have two different temperatures inside the plasma. In order to determine which solution is physical, we employ two boundary conditions: (i) The flow rate passing through the hot region should not exceed the total flow rate of the experiment, and (ii) the plasma temperature and NO_x concentration as a function of current and flow rate must agree with the experimental observations. The plasma temperature and the flow rate passing through the region with elevated temperature, obtained according to these calculations, are plotted in Figure 16 as a function of current, for different flow rates, for 14 cm distance between both electrodes.

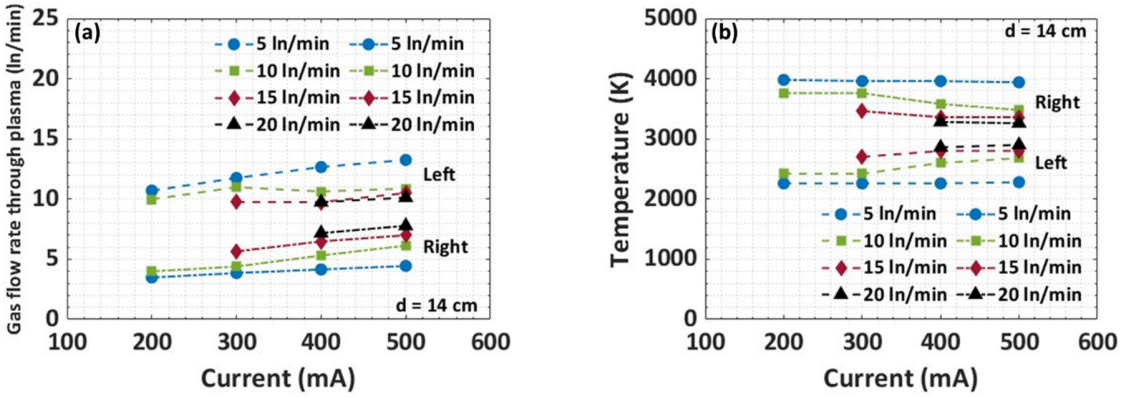

Figure 16. Calculated flow rate passing through the region with elevated temperature (a), and corresponding plasma temperatures (b), in the small reactor, as a function of current for four different flow rates, for 14 cm distance between both electrodes. "Left" and "right" in the figure denote whether the values of temperature are taken from the left-hand side or right-hand side of the EC graph (Figure 14 b); see text.

Our calculations show that if we take the values of the temperature from the right-hand side of the EC graph (Figure 14 b), as presented by the dash-dotted curves in Figure 16, all flow rates calculated in this way are below the total flow rate. If we take the values from the left-hand side of the graph, the calculations for 5 and 10 ln/min provide unphysical results, being higher than the total flow rate, while the calculations for 15 and 20 ln/min predict flow rates below the total flow rate, hence they are physical (Figure 16 a). Only looking at the flow rate, we cannot determine which conditions are physical, and we need to look at the temperatures and NO_x concentration as well.

We can see from Figure 16 b that if we take the values of the EC from the right-hand side of the plot in Figure 14 b, the temperature slightly decreases as a function of current (mainly at 10 ln/min), while for the values at the left-hand side, the temperature slightly increases as a function of current (again mainly at 10 ln/min; see Figure 16 b). From our experiments we know that the EC in the small reactor decreases with increasing SEI (Figure 7 a), which means that the temperature and the NO_x concentration have to increase with current. The latter also corresponds to our expectations and the general understanding of arc plasmas. This means that we are on the left-hand side of the EC graph.

Taking these effects into account, we can see that only the flow rates of 15 and 20 ln/min satisfy these conditions. As seen from Figure 5, the plasma is less contracted at low gas flow rate, where we can consider that the power is deposited within the whole reactor and the back-reactions are limiting the conversion, while at the higher gas flow rates, when the plasma is contracted, our approximations become more valid, i.e., (i) the plasma is thermally insulated, and (ii) the cold gas surrounding the plasma stops the back-reactions through mixing, and all products generated in the hot region are recovered (see discussion above). Our model shows that, provided the above assumptions are valid, a value of the EC near the thermodynamic limit can be reached, but at the expense of dilution of the produced NO_x; in other words, at a lower NO_x concentration than predicted by the model.

4.8. Application of the same method to the large reactor

Based on the above assumptions, we can now also roughly describe the behavior of the large pin-to-pin reactor. Indeed, in this situation the plasma is always contracted, and the NO_x concentration is also increasing with current.

Following our previous considerations, the plasma temperature must be taken from the left-hand side of the EC graph (Figure 14 b). Figure 17 presents the calculated plasma temperature and flow rate passing through the region with elevated temperature for the large pin-to-pin reactor with 14 cm distance between both electrodes, as a function of current for three different flow rates.

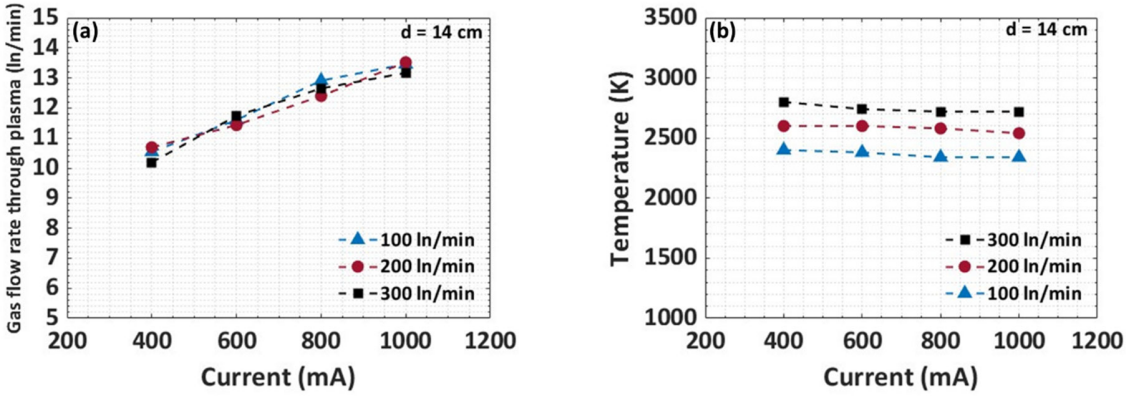

Figure 17. Calculated flow rate passing through the region with elevated temperature (a) and corresponding plasma temperature (b), in the large pin-to-pin reactor with 14 cm distance between both electrodes, as a function of current, for different flow rates.

We can see that the flow rate through the region with elevated temperature increases with current and is nearly the same as what we calculated for the smaller reactor (cf. Figure 16 a and Figure 17 a) for 400 mA, despite the much larger reactor dimension, hence indicating indeed that the plasma is significantly contracted in the large reactor. Upon rising current, the radius of the plasma rises, which leads to a 4 ln/min increase in flow rate passing through the plasma for 1000 mA. Nevertheless, this flow rate of 14 ln/min is still dramatically lower than the experimental flow rates, due to the contract nature of the plasma. Note that the flow rate passing through the plasma is roughly the same for a total flow rate of 100, 200 and 300 ln/min.

The calculated temperature in the plasma is also very similar to the values determined in the small reactor (cf. Figure 16 b (left) and Figure 17 b), increasing as a function of flow rate, but in this case slightly decreasing as a function of current. This behavior highlights the limitation of our approach. In the large reactor (low SEI region), the measured EC increases as a function of SEI, together with the NO_x concentration (cf. Figure 10). There are only two ways for the EC to increase as a function of SEI: (i) if we follow the left-hand side of the EC graph (Figure 14 b), the temperature has to drop with increasing NO_x concentration, or (ii) if we follow the right-hand side of that graph, the temperature has to increase, and the NO_x concentration should drop. In our experiments, we observe an increase in both EC and NO_x concentration as a function of SEI. Following Figure 14 a, this would mean that the back-reactions are dominating and are limiting the conversion. Hence, one of our main assumptions breaks down and we observe a decreasing temperature as a function of current. This indicates that the design of the large pin-to-pin reactor must be improved in order to reach higher NO_x concentrations for low EC, due to the limitations of the back-reactions. Indeed, if the model breaks down, it means that the reactor does not operate efficiently.

Increasing the SEI in the large reactor (by applying a higher power) will only yield better performance if the plasma column would also become broader; otherwise, there is still a lot of gas not passing through the plasma and diluting the produced NO_x. However, a higher plasma power will not necessarily lead to a wider plasma column, due to the natural phenomenon of contraction at high power plasmas. We plan to test this in our future work. Despite this, we can see from Figure 17 b that the drop in temperature as a function of current is not very large, so we believe that the information extracted is still valuable for comparing the results between the different reactors, especially for the low EC conditions, where our approximations should be more valid.

The same evaluation is also made for the large reactor in torch configuration. The flow rate passing through the region with elevated temperature and the plasma temperature as a function of current for three different flow rates in the torch configurations are presented in Figure 18.

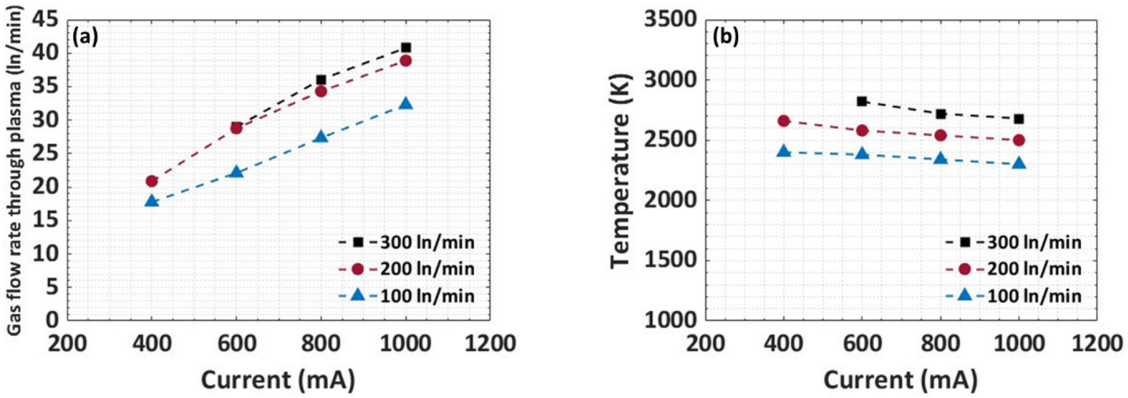

Figure 18. Calculated flow rate passing through the region with elevated temperature (a) and corresponding plasma temperature (b), as a function of current, for different flow rates for the torch configuration.

The torch configuration clearly provides better performance than the pin-to-pin reactor. The flow rate passing through the plasma is significantly higher, reaching nearly 30 ln/min for 100 ln/min total flow rate, and 40 ln/min for 300 ln/min total flow rate, both at the highest current, while the plasma temperature slightly drops as a function of current. This indicates that this torch design is suitable for upscaling, provided that the temperature after the plasma can drop sufficiently fast to avoid back-reactions (recombination of NO with O or N atoms). As mentioned in previous section, removing the bottom electrode allows the arc to freely glide and rotate within the reactor, leading to a larger fraction of the gas heated to the desirable temperature. Despite this, the plasma is still relatively contracted, and thus, still a very small fraction of the gas is heated compared to the increase in flow rate that we have provided (i.e., only 30 – 40 ln/min, for a

total flow rate of 100 – 300 ln/min; cf. Figure 18 a). These results clearly indicate that the limited NO_x concentration in the large reactor is not caused by the chemistry, but by the fluid dynamics and plasma phenomena influencing the process.

The exact mechanisms of how the mixing process results in quenching of the back-reactions is a complicated computational fluid dynamics problem, which will be addressed in our future research. However, similar observations were made by D'Isa et al., in a CO_2 microwave plasma in the low SEI region, where the thermodynamic limit was also reached [48]. We note that Birkland also reached to similar conclusions related to the plasma dynamics and the process of plasma-based NF. In order to operate their reactor efficiently, only ¼ of the gas had to pass through the plasma and the remaining ¾ acted as quenching gas. As a result, their NO concentration was lower but produced quite efficiently[6,7], just like in our upscaled reactor.

In general, our study shows that plasma reactors can be very efficiently scaled up, provided that the concentration of products is lower than the maximum based on thermodynamic equilibrium. Indeed, our model assumes that mixing of the unreacted gas with the produced NO_x stops the back-reactions. We see that our model breaks down at the conditions of the large reactor, which indicates that back-reactions become too important. This is attributed to poor mixing between the gas surrounding the plasma and the hot gas inside the plasma, because there is so much gas surrounding the plasma in the large reactor, which is not in close contact with the hot plasma core.

4.9. Summary of the insights obtained from the thermodynamic equilibrium calculations

Our thermodynamic equilibrium calculations show that we have almost reached the thermodynamic limit of the EC (estimated as 2.74 MJ/mol for NO_x production from air) in the small reactor, as well as in the large reactor, both in pin-to-pin and torch configuration. However, the contracted nature of the plasma leads to measured NO_x concentrations that are much lower than those predicted by the thermodynamic equilibrium calculations, due to dilution with non-reacted gas. Despite this, the fact that we are reaching EC values near the calculated thermodynamic minimum indicates that the same process responsible for the low concentrations (i.e., dilution with non-reacted gas) is also responsible for the low EC, because this dilution stops possible back-reactions. Our model can also give an explanation on why the trends of EC as a function of SEI differ between the small and large reactor. The possible reason for this could be the flow pattern and slight geometry difference between the reactors, which in turn leads to faster mixing in the small reactor as compared to the large reactor. These insights can help us to design better upscaled reactors, overcoming these limitations. Finally, based on these thermodynamic calculations, we propose a method to estimate the plasma temperature and flow rate passing through the plasma. Our model illustrates that the

flow rate passing through the plasma in the torch configuration is already significantly higher than in the pin-to-pin reactor, explaining the higher NO_x concentrations achieved in our experiments. We believe this can provide a strategy to further improve energy-efficient upscaling of plasma-based NO_x production, as well as other plasma-based gas conversion applications.

As a final note, in our method, we don't need to define a plasma volume in order to calculate the flow passing through the plasma. In fact, defining the plasma volume is difficult, and would be based on a lot of assumptions and uncertainties. For example, one needs to know the gas flow pattern in the reactor and the precise plasma diameter, which in itself also depends on the gas flow dynamics, thus requiring detailed CFD simulations, because experimental measurements up to now cannot yet reveal the exact flow dynamics. In contrast, our calculations allow us to estimate the mass flow passing through the plasma based on the theoretical EC calculated assuming thermodynamic equilibrium, hence, without the need to know the plasma volume.

5. Conclusions

Plasma-based NO_x production is promising for fertilizer applications, but a major challenge is to maintain the high NO_x concentration and low EC when upscaling the reactor. Hence, in this work we tried to tackle this challenge by developing a low current, high flow rate plasma reactor, and we compare the results with its smaller counterpart, operating according to the same principle (pin-to-pin reactor, powered by DC current, operating in the arc regime), but at lower flow rates. This allows us to scan a large range of SEI values and investigate the potential of reactor upscaling.

Experimentally, we studied the plasma-based NO_x production as a function of current and flow rate, ranging from 200 to 1000 mA and from 5 to 300 ln/min, respectively, for a small pin-to-pin reactor, a large pin-to-pin reactor, as well as the same reactor but in torch configuration, to overcome the limitations in upscaling of the pin-to-pin reactor. Varying the current and flow rate, together with operating the reactor at different configurations, indeed allowed us to study the plasma-based NO_x production in a wide range of SEI, i.e., between 0.1 and 7.6 kJ/l.

We showed that the EC and NO_x concentration depend on SEI, but also on the flow rate in conjunction with the interelectrode distance. The lowest EC achieved in our study was 2.8 MJ/mol, for an NO_x concentration of 1.72% at a flow rate of 20 ln/min and distance between the electrodes of 14 cm, for the small reactor. The highest NO_x concentration obtained in this reactor is 3.51%, but corresponding to an EC of 4.8 MJ/mol. Note that these results were obtained for NO_x production simply from air, and that in oxygen-enriched air, the results are typically better. Care should be taken when comparing the results with literature (cf. Figure 1 in the introduction), where the best results are typically reported for oxygen-enriched air. However, we

want to design an industrial process, where starting from air is more convenient, and otherwise the cost of producing oxygen-enriched air should also be accounted for, which is never done in literature.

In the large reactor with the same design (pin-to-pin), the NO_x concentration drops dramatically to 0.21%, for an EC of 4.5 MJ/mol, due to the much higher flow rate. The lowest EC in this configuration is 2.9 MJ/mol, for an NO_x concentration of only 0.11%. Due to this lower NO_x concentration, the PR is very similar as in the small reactor, despite the much higher flow rate. The reason for this is the contracted nature of the plasma, which results in producing low NO_x concentrations due to dilution of the produced NO_x with unreacted gas that has not passed through the plasma, but it improves the EC due to quenching of the back-reactions.

On the other hand, when changing the large reactor to a torch configuration, the NO_x concentrations are more than double the values obtained in the pin-to-pin reactor, for nearly the same EC. This illustrates the potential for upscaling this technology. Indeed, we achieved production rates of 80 g/h for an EC of 2.9 MJ/mol with this torch configuration, at a flow rate of 300 ln/min. This is ca. three times higher than the production rate in the small reactor. Operating the large reactor in the torch configuration leads to a larger amount of gas treated by the plasma, by changing the arc geometry. Indeed, the arc (plasma) can now freely glide inside the reactor, and thus, fill a larger reactor volume, as compared to the pseudo-cylindrical column in the pin-to-pin configuration. This enhances the performance of the reactor, demonstrating that the torch configuration is a better suited design for scale up, due to the somewhat larger plasma column, filling a larger fraction of the reactor volume, so that higher flow rates can pass through the plasma, as demonstrated by our calculations. Based on our previous research, increasing the pressure inside the reactor will substantially increase the NO_x concentration and should bring the process much closer to industrial applications [27].

Last but not least, we showed based on thermodynamic equilibrium calculations that we have nearly reached the thermodynamic minimum of the EC (i.e., 2.74 MJ/mol for NO_x production from air; note that it is lower for oxygen-enriched air). However, due to the contracted nature of the plasma, the measured NO_x concentrations are significantly lower than those predicted by the thermodynamic equilibrium calculations, due to the dilution with non-reacted gas, as mentioned above. In reality, the process is strongly dependent on the SEI effectively delivered to the plasma, rather than the overall (macroscopic, measured) SEI delivered to the reactor, which leads to the false impression that a lower macroscopic SEI (at constant NO_x concentration) should lead to a lower EC. Indeed, this lower macroscopic SEI can correspond to a high SEI inside the plasma, due to the contract nature of the plasma. The presented thermodynamic calculations allow us to estimate the plasma temperature and flow rate passing through the plasma, based on the measured products. It can explain the better performance of the torch configuration, due to the larger flow

rates passing through the plasma. This provides a strategy for potential energy-efficient scale up of the technology.

Conflicts of interest

There are no conflicts to declare.

Acknowledgments

This research was supported by a bilateral agreement with N2 Applied, the European Research Council (ERC) under the European Union's Horizon 2020 research and innovation programme (grant agreement No. 810182 – SCOPE ERC Synergy project, and grant agreement No. 101081162 – PREPARE ERC Proof of Concept project), as well as by the Excellence of Science FWO-FNRS project (FWO grant ID GoF9618n, EOS ID 30505023) and the Fund for Scientific Research (FWO) Flanders Bio-economy project (grant № G0G2322N), funded by the European Union – NextGenerationEU.

Notes and References

1 B. S. Patil, Q. Wang, V. Hessel and J. Lang, *Catal. Today*, 2015, **256**, 49–66.

2 R. Snoeckx and A. Bogaerts, *Chem. Soc. Rev.*, 2017, **46**, 5805–5863.

3 A. Bogaerts and E. C. Neyts, *ACS Energy Lett.*, 2018, **3**, 1013–1027.

4 J. Li, S. Yao and Z. Wu, *J. Phys. D. Appl. Phys.*, , DOI:10.1088/1361-6463/ab946a.

5 K. H. R. Rouwenhorst, F. Jardali, A. Bogaerts and L. Lefferts, *Energy Environ. Sci.*, 2021, **14**, 2520–2534.

6 K. H. R. Rouwenhorst, F. Jardali, A. Bogaerts and L. Lefferts, *Energy Environ. Sci.*, 2023, **16**, 6170–6173.

7 J. Liu, L. Nie, D. Liu and X. Lu, *Plasma Process. Polym.*, 2024, **21**, 2300153.

8 S. Eyde, *J. Ind. Eng. Chem.*, 1912, **4**, 771–774.

9 K. Birkeland, *Trans. Faraday Soc.*, 1906, **2**, 98–116.

10 I. Krop, J.; Pollo, *Chemia*, 1981, **678**, 51–59.

11 W. Bian, X. Song, J. Shi and X. Yin, *J. Electrostat.*, 2012, **70**, 317–326.

12 H. Patel, R. K. Sharma, V. Kyriakou, A. Pandiyan, S. Welzel, M. C. M. van de Sanden and M. N. Tsampas, *ACS Energy Lett.*, 2019, **4**, 2091–2095.

13 A. V Pipa, T. Bindemann, R. Foest, E. Kindel, J. Röpcke and K.-D. Weltmann, *J. Phys. D. Appl. Phys.*, 2008, **41**, 194011.

14 X. Pei, D. Gidon, Y.-J. Yang, Z. Xiong and D. B. Graves, *Chem. Eng. J.*, 2019, **362**, 217–228.

15 B. S. Patil, N. Cherkasov, J. Lang, A. O. Ibhadon, V. Hessel and Q. Wang, *Appl. Catal. B Environ.*, 2016, **194**, 123–133.

16 Q. Sun, A. Zhu, X. Yang, J. Niu and Y. Xu, *Chem. Commun.*, 2003, 1418–1419.

17 A. A. Abdelaziz and H.-H. Kim, *J. Phys. D. Appl. Phys.*, 2020, **53**, 114001.

18 D. Rapakoulias, S. Cavadias and J. Amouroux, *Rev. Phys. Appl.*, 1980, **15**, 1261–1265.

19 B. Mutel, O. Dessaux and P. Goudmand, *Rev. Phys. Appliquée*, 1984, **19**, 461–464.

20 R. I. Asisov, V. K. Givotov, V. D. Rusanov and A. Fridman, *Sov. Phys.*, 1980, **14**, 366.

21 F. B. Polak, L. S., Ovsiannikov, A. A., Slovetsky, D. I. & Vurzel, *Theoretical and Applied Plasma Chemistry*, Physical Society of the GDR, German Democratic Republic, 1975.

22 E. Vervloessem, Y. Gorbanev, A. Nikiforov, N. De Geyter and A. Bogaerts, *Green Chem.*, 2022, **24**, 916–929.

23 M. Janda, V. Martišovitš, K. Hensel and Z. Machala, *Plasma Chem. Plasma Process.*, 2016, **36**, 767–781.

24 M. J. Pavlovich, T. Ono, C. Galleher, B. Curtis, D. S. Clark, Z. Machala and D. B. Graves, *J. Phys. D. Appl. Phys.*, 2014, **47**, 505202.

25 F. Jardali, S. Van Alphen, J. Creel, H. Ahmadi Eshtehardi, M. Axelsson, R. Ingels, R. Snyders and A. Bogaerts, *Green Chem.*, 2021, **23**, 1748–1757.

26 S. Van Alphen, H. A. Eshtehardi, C. O'Modhrain, J. Bogaerts, H. Van Poyer, J. Creel, M.-P. Delplancke, R. Snyders and A. Bogaerts, *Chem. Eng. J.*, 2022, **443**, 136529.

27 I. Tsonev, C. O'Modhrain, A. Bogaerts and Y. Gorbanev, *ACS Sustain. Chem. Eng.*, 2023, **11**, 1888–1897.

28 E. Vervloessem, M. Aghaei, F. Jardali, N. Hafezkhiabani and A. Bogaerts, *ACS Sustain. Chem. Eng.*, 2020, **8**, 9711–9720.

29 X. Hao, A. M. Mattson, C. M. Edelblute, M. A. Malik, L. C. Heller and J. F. Kolb, *Plasma*

Process. Polym., 2014, **11**, 1044–1056.

30 Y. D. Korolev, O. B. Frants, N. V Landl and A. I. Suslov, *IEEE Trans. Plasma Sci.*, 2012, **40**, 2837–2842.

31 R. Ingels, *Energy efficient process for producing nitrogen oxide, Norw*, Norway, 2012.

32 X. Y. Lei, H. Cheng, L. L. Nie and X. P. Lu, *Plasma Chem. Plasma Process.*, 2022, **42**, 211–227.

33 B. S. Patil, F. J. J. Peeters, G. J. van Rooij, J. A. Medrano, F. Gallucci, J. Lang, Q. Wang and V. Hessel, *AIChE J.*, 2018, **64**, 526–537.

34 S. Kelly and A. Bogaerts, *Joule*, 2021, **5**, 3006–3030.

35 T. Kim, S. Song, J. Kim and R. Iwasaki, *Jpn. J. Appl. Phys.*, , DOI:10.1143/JJAP.49.126201.

36 X. Pei, D. Gidon and D. B. Graves, *J. Phys. D. Appl. Phys.*, , DOI:10.1088/1361-6463/ab5095.

37 N. Cherkasov, A. O. Ibhadon and P. Fitzpatrick, *Chem. Eng. Process. Process Intensif.*, 2015, **90**, 24–33.

38 R. Snoeckx and A. Bogaerts, *Chem. Soc. Rev.*, 2017, **46**, 5805–5863.

39 Y. P. Raizer, *Gas discharge physics*, Springer-Verlag Berlin Heidelberg, Berlin, 1991.

40 G. V Naidis, *Plasma Sources Sci. Technol.*, 2007, **16**, 297.

41 COMSOL Multiphysics® v. 6.0, COMSOL AB: Stockholm, Sweden.,

42 N L Aleksandrov, E M Bazelyan, I V Kochetov and N A Dyatko, *J. Phys. D. Appl. Phys.*, 1997, **30**, 1616.

43 D. L. Baulch, C. T. Bowman, C. J. Cobos, R. A. Cox, T. Just, J. A. Kerr, M. J. Pilling, D. Stocker, J. Troe, W. Tsang, R. W. Walker and J. Warnatz, *J. Phys. Chem. Ref. Data*, 2005, **34**, 757–1397.

44 B. J. . McBride, M. J. . Zehe and S.Gordon, *NASA Glenn Coefficients for Calculating Thermodynamic Properties of Individual Species; National Aeronautics and Space Administration*, Cleveland, MD, USA, 2002.

45 Z. Machala, C. Laux, C. Kruger and G. Candler, in *42nd AIAA Aerospace Sciences Meeting and Exhibit*, American Institute of Aeronautics and Astronautics, 2004.

46 I. Tsonev, J. Boothroyd, S. Kolev and A. Bogaerts, *Plasma Sources Sci. Technol.*, 2023, **32**, 54002.

47 T. Nunnally, K. Gutsol, A. Rabinovich, A. Fridman, A. Gutsol and A. Kemoun, *J. Phys. D. Appl. Phys.*, 2011, **44**, 274009.

48 F. A. D'Isa, E. A. D. Carbone, A. Hecimovic and U. Fantz, *Plasma Sources Sci. Technol.*, 2020, **29**, 105009.